**CONSTRAINTS ON DYNAMIC TOPOGRAPHY FROM ASYMMETRIC SUBSIDENCE**

**ACROSS THE MID-OCEAN RIDGES**

A THESIS SUBMITTED TO THE GRADUATE DIVISION OF THE UNIVERSITY OF HAWAIʻI

AT MĀNOA IN PARTIAL FULFILLMENT OF THE REQUIREMENTS FOR THE DEGREE OF

**MASTER OF SCIENCE**

IN

**GEOLOGY & GEOPHYSICS**

JUNE 2016

By

**C. EVAN WATKINS**

Thesis Committee:

Clinton P. Conrad, Chairperson

Paul Wessel

Neil Frazer

Keywords: Dynamic topography, mantle dynamics, bathymetry, ridge asymmetry

## Acknowledgments

**Abstract**

Stresses from mantle convection should deflect Earth's surface vertically, with important implications for continental dynamics and sea-level change. However, dynamic topography is difficult to observe directly because it is obscured by isostatic topography. As a result, amplitudes of long wavelength dynamic topography inferred from indirect observations tend to differ significantly from model predictions. In this study we attempt to resolve this discrepancy by analyzing asymmetries in seafloor bathymetry across mid-ocean ridges, which in the absence of dynamic topography should otherwise be symmetrical. We identify dynamic deflections of the seafloor by focusing on seafloor unperturbed by volcanism on both sides the Mid-Atlantic Ridge and the East Pacific Rise. Across both ridges the magnitude of the subsidence is greater on the South American side of the ridge, consistent with patterns predicted by numerical models of long-wavelength dynamic topography. To constrain the amplitude of dynamic topography, we compare bathymetric profiles across both ridges after correcting bathymetry for several different models of dynamic topography with varying amplitudes and spatial patterns. We found that the observed asymmetry in both ridge systems is best explained if bathymetry is deflected by dynamic topography with long-wavelength amplitudes of about 300-500 m, which is about half of the amplitudes predicted by recent mantle flow models. This reduction in amplitude implies that long-wavelength mantle flow is driven primarily by active downwelling associated with subducted slabs in the lower mantle, and less so by active upwelling. This pattern of mantle dynamics is consistent with recent thermochemical convection models of mantle flow.

**Table of Contents**

# List of Figures

## 1. Introduction

Convective flow in the mantle supports deflections of Earth's solid surface known as dynamic topography [*Hager et al.*, 1985]. Changes in this dynamic topography, which result from the time-dependence of mantle flow, have been identified as exerting important controls on sea level change [e.g., *Conrad and Husson*, 2009; *Moucha et al.*, 2008; *Spasojevic and Gurnis*, 2012] and continental dynamics [e.g., *Lithgow-Bertelloni and Silver*, 1998; *L Liu*, 2015; *Shephard et al.*, 2012] over timescales of millions of years. However, our understanding of the influence of dynamic topography is complicated by significant uncertainties over its amplitude. In particular, constraints on the long wavelength (~$10^4$ km in width) component of dynamic topography range from about one hundred meters based on observational studies [e.g., *Molnar et al.*, 2015; *Winterbourne et al.*, 2014] to upwards of one kilometer from mantle flow models [e.g., *Conrad*, 2013; *Flament et al.*, 2013; *Hager et al.*, 1985; *Moucha et al.*, 2008; *Spasojevic and Gurnis*, 2012; *Steinberger*, 2007]. To constrain these uncertainties, we look for the signature of dynamic topography within bathymetric observations of seafloor subsidence away from mid-ocean ridges [e.g., *Zhong et al.*, 2007].

Numerical mantle flow models driven by mantle density heterogeneity predict vertical stresses that support dynamic topography at the Earth's surface. For a given mantle viscosity structure, the amplitude of long wavelength dynamic topography is largely controlled by the conversion factor, $R = \delta \ln(\rho)/\delta \ln(Vs)$, that translates a seismic velocity anomaly to a mantle density anomaly. Typical theoretical values of $R$ range from 0.15 to 0.4 for most of the mantle, with uncertainty associated with the relationship between the thermal expansion coefficient, temperature, density, pressure, and composition [e.g., *Bull et al.*, 2010; *Gurnis et al.*, 2000; *Karato and Karki*, 2001]. Previous studies have applied a constant value of $R$ for the whole mantle [e.g., *Conrad and Husson*, 2009; *Steinberger et al.*, 2001], a constant $R$ throughout the upper mantle and a depth varying $R$ in the lower mantle [e.g., *Cammarano et al.*, 2003], and near-zero or negative values of $R$ for the seismically

slow regions in the lowermost mantle [e.g., *Matas and Bukowinski*, 2007]. Plate velocities and the balance of plate-driving forces also constrain the seismic conversion factor, but this constraint is complicated by uncertainty associated with the mantle's viscosity structure [e.g., *Becker and O'Connell*, 2001; *Steinberger et al.*, 2001; *van Summeren et al.*, 2012]. The seismic conversion factor may also differ between positive and negative seismic velocity anomalies in the mantle. In particular, the large low-shear-velocity provinces (LLSVPs) in the lowermost mantle have been attributed to thermal effects, compositionally distinct materials, or a mix of factors [*Deschamps et al.*, 2015; *McNamara et al.*, 2010], all of which imply different distributions of mantle density heterogeneity [*Austermann et al.*, 2014; *Bower et al.*, 2013; *Flament et al.*, 2013; *Shephard et al.*, 2014], and thus different amplitudes for associated dynamic topography [*Liu and Zhong*, 2016].

Observational constraints on the amplitude and pattern of dynamic topography could potentially help to resolve these uncertainties, and thus place new constraints on mantle processes. However, dynamic topography is difficult to observe directly. Over the continents, larger-amplitude isostatic topography from crustal density variations obscures long wavelength dynamic topography of the surface. One approach for detecting the component of topography that is dynamically supported is to use free-air gravity anomalies, which should be zero for isostatically-supported topography. For long wavelengths, estimates of the admittance, which converts free-air gravity anomalies to dynamic topography, are uncertain and range from near zero or even negative values [*Colli et al.*, 2016] up to ~143 mgal/km for orogenous zones [*Molnar et al.*, 2015]. Such values correspond to dynamic topography with amplitudes ranging from the kilometer scale to negligible [e.g., *Molnar et al.*, 2015; *Winterbourne et al.*, 2014]. Furthermore, *Crosby* [2007] analyzed synthetic data to show that uncertainty in gravitational admittance increases at long wavelength and *Revenaugh and Parsons* [1987] predict from theoretical arguments that admittance significantly decreases for long wavelength structures. This suggests the potential for large dynamic topography without large free-

air gravity anomalies [*Colli et al.*, 2016], but does not help to constrain the actual amplitude of dynamic topography.

In contrast, half-space cooling of young seafloor follows a well-understood subsidence pattern that allows us to predict isostatic topography in a relatively straightforward way. In particular, as seafloor moves away from the mid-ocean ridges, it passively cools, thickens, and subsides such that seafloor depth increases as the square root of seafloor age [e.g., *Parsons and Sclater*, 1977]. Furthermore, this subsidence of isostatic topography of the seafloor should occur symmetrically on both sides of the mid-ocean ridge (MOR). Hence, if seafloor is deflected over long wavelengths by dynamic topography, we would expect to observe an asymmetry in subsidence rates across the MOR (Figure 1). Here we examine subsidence trends across large areas of young seafloor in the Pacific and Atlantic basins, and use the resulting observations of subsidence asymmetry to develop a new constraint on the amplitude of dynamic topography.

## 2. Detecting Ridge Flank Asymmetry

To constrain the amplitude of dynamic topography, we utilize satellite constraints on ocean floor bathymetry from the ETOPO1 model of the ocean bathymetry sampled at a spacing of a tenth of a degree, or roughly 9-15km [*Sandwell and Smith*, 2009]. This dataset contains points constrained by both shiptrack bathymetry and satellite gravity observations. [*Sandwell and Smith*, 2009]. Then, to examine areas relatively unperturbed by local phenomena, we removed the bathymetric signal of large igneous provinces (LIPs) by utilizing the *Coffin and Eldholm* [2005] global map of LIPs and extending LIP edges by 100km (figure 2a). We used the Global Seamount Census of *Kim and Wessel* [2011] to mask seafloor within three times the major axis of all seamounts greater than one kilometer in height (Fig. 2a). Varying the masking radii from two to five times the major radius did not significantly impact our results. Because seafloor sediments also impact bathymetry

[*Winterbourne et al.*, 2014], we excluded areas with more than one kilometer of sediment (black areas in Fig. 2b), then isostatically compensated sediments in the remaining areas using the updated NGDC Ocean Sediment map [*Whittaker et al.*, 2013] and the isostatic formulation of *Sykes* [1996]. Abyssal hill processes generate another natural source of variability in depth measurements. We minimized the potential for aliasing, where the natural abyssal hill spacing of 20-100 kyr is smaller than grid mesh for the sampled surface, by applying a 25 km Gaussian filter using the Generic Mapping Tools and by binning and bootstrapping the bathymetry within an age range in order to have enough samples to average out abyssal hills and other geological anomalies along the age profile [*Olive et al.*, 2015; *Wessel et al.*, 2013].

In order to assess the potential bathymetric asymmetry of MORs, we analyzed the central Mid-Atlantic Ridge (MAR) and East Pacific Rise (EPR) (white outlines in Fig. 2), as other regions of the MORs exhibit intense volcanic activity, highly asymmetric age distribution, or complex geometry. For the EPR, we examined seafloor younger than 40 Ma so that profiles would include seafloor on both sides of the ridge. In the Atlantic Basin, we used an age cutoff of 70Ma to ensure that the dominant physical process would be half-space cooling and not seafloor flattening processes that become important for seafloor older than ~80 Ma [*Stein and Stein*, 1992]. We limited the North-South range of the Atlantic Basin to between 30°N and 40°S to minimize the impact of the Icelandic plume.

In order to develop a robust linear regression of bathymetry as a function of the square root of the age of the seafloor, we bootstrapped the bathymetric data by the square root of age by randomly selecting an equal number of data points for each of the 70 and 120 equally spaced in the square root of age bins for the EPR and MAR, respectively. This mitigates the inherent sampling bias toward younger seafloor [*Korenaga and Korenaga*, 2008]. We performed a simple least-squares linear regression of depth versus the square root of age globally over the age range of 5 to 70 Ma

and on each of the four ridge flanks studied. Applying this method globally and using 1000 points in each of the bins, we found a subsidence rate for ages <70Ma of $319\pm24$ m/ma$^{1/2}$, which agrees with the rate of $315\pm26$ m/Ma$^{1/2}$ previously reported by *Korenaga and Korenaga* [2008]. We also tested the results for young seafloor using ETOPO1 against the shiptrack-constrained bathymetry and found negligible difference [*Sandwell and Smith*, 2009].

Both the Pacific and Atlantic basins showed a disparity of slope across the MOR with the South American side being steeper, as predicted by numerical models of dynamic topography (Fig. 3a) [e.g., *Conrad and Husson*, 2009; *Flament et al.*, 2013; *Moucha et al.*, 2008]. The difference in subsidence rate was pronounced but more poorly constrained across the EPR ($50\pm10$ m/Ma$^{1/2}$) than across the MAR ($17\pm4$ m/Ma$^{1/2}$) (Fig. 8). Additionally, linear fits to the bathymetry produce a difference in the mean ridge height offset between opposite ridge flanks. This difference amounts to $100\pm200$ m and $200\pm400$ m across the MAR and EPR respectively, where the South American side is deeper for the MAR and shallower for the EPR.

## 3. Dynamic Topography

We considered dynamic topography as an explanation for the apparent asymmetries across the MAR and EPR. For this we used predictions of dynamic topography from the global mantle flow models of *Conrad and Husson* [2009] (Fig. 3a). This modeled dynamic topography is similar in amplitude and long-wavelength pattern to dynamic topography predicted by several other global mantle flow models [e.g., *Flament et al.*, 2013; *Hager et al.*, 1985; *Moucha et al.*, 2008], as reviewed recently by *Flament et al.* [2013]. The models of *Conrad and Husson* [2009] were developed using a spherical finite element code [CitcomS, *Tan et al.*, 2006; *Zhong et al.*, 2008] that assumes a linear viscosity, where flow-fields driven by positive or negative density anomalies were computed separately and based on the seismic S-wave tomography model S20RTSb [*Ritsema et al.*, 2004]. Their

mantle flow models ignored velocity anomalies in the top 300 km of the mantle due to concerns associated with continental roots. Global patterns of dynamic topography (Fig. 3a) exhibit minima surrounding Southeast Asia and South America, and maxima across the South Pacific super-swell and Africa, mirroring the areas of long-term subduction along the margins of the Pacific Basin and the LLSVPs in the deep mantle, respectively. Because they assumed a linear rheology, *Conrad and Husson* [2009] separated mantle flow into four components driven by different sets of density anomalies in the mantle. In particular, they computed dynamic topography supported by mantle flow driven by high-density (Figs. 3C and 3E) and low-density anomalies (Figs. 3B and 3D), which produce active downwelling and upwelling, respectively, in both the upper (Figs. 3B and 3C) and lower mantle (Figs. 3D and 3E). These four components result in separate models of mantle flow that predict four different patterns of dynamic topography, which we then normalized (Figs. 3B-3D). We use these dynamic topography basis functions (DTBF) to constrain the amplitude of dynamic topography that minimizes the observed ridge flank asymmetries (Figs. 4b and 5b).

To constrain the impact of dynamic topography on ridge asymmetry we produced a set of dynamic topography models by multiplying each of the four DTBFs by a range of peak amplitudes. In doing so, we effectively explore a range of potential seismic conversion factors, $R$, for each of the four sources of density anomaly. The resulting models produce dynamic topography with peak amplitudes ranging from $-500$ meters (corresponding to a negative $R$) to 1500 meters (corresponding to a large positive $R$). We subtracted the resulting prediction of dynamic topography from the regional residual topography across the MAR and EPR and assessed the resulting bathymetric asymmetry across these ridges.

**4. Statistical Constraints on the Amplitude of Dynamic Topography**

After correcting seafloor bathymetry for a given model of dynamic topography, we quantify basin asymmetry by comparing the square root of age linear regressions for both ridge flanks (left columns of Figs. 4 and 5). We use the South American side of each ridge flank (solid black lines in Figs. 4 and 5) as a reference against which to compare trends for the opposite ridge flank (dashed blue lines). We then test for symmetry across the MAR (Fig. 4) and EPR (Fig. 5) by comparing the distribution of data from both sides of the ridge flank. To make this differentiation, we compare histograms (right columns of Figs. 4 and 5) that show the distribution of the bathymetric difference of each point on both sides of the basin relative to the regression developed for the South American flank. As the histogram is another representation of the fitting, the distribution for the South American flank is centered about zero (black line in right columns of Figs. 4 and 5), but the mean of the distribution for the opposing flank (vertical blue dashed line in the right columns of Figs. 4 and 5) will only be close to zero if the ridge is bathymetrically symmetrical.

To quantify the degree of symmetry across the MOR, we employ the two-sample Kolmogorov–Smirnov (K-S) test [*Oliphant*, 2007], which uses the difference in the empirical cumulative distribution functions (CDF), and thus is sensitive to differences in both the position and shape of the two distributions. The maximum difference between the CDF of the two distributions is directly related to the p-value that quantifies the probability that the two distributions are sampled from the same source function. Thus, solutions with p-values less than 0.05 (black horizontal lines in Fig. 6) likely indicate ridge asymmetry, because the distributions are distinguishable from one another with 95% confidence.

The P-value is also a function of the number of samples in the distribution, and thus of how we bootstrapped the data. However, the appropriate number of independent samples of seafloor is not known. From previous studies of global bathymetry [*Korenaga and Korenaga*, 2008], the inherent

variability of seafloor depth is on the order of $\pm400$ m (as shown in the shaded areas of Figs. 4 and 5) and most seafloor depth grid points are not independent from each other as the bathymetric data are not measured systematically with age or geological trend, but is instead spatially derived from gridded satellite gravity observations [*Sandwell and Smith*, 2009]. Therefore, we vary the number of independent samples per age bin ($N_{bin}$) from 10 to 1000 samples per square-root of age bin (Fig. 6), a range of bin sizes that runs from undersampling to oversampling the bathymetry data. This range relates to the natural length scales of bathymetry variations in the ocean and also to the bootstrapping process, which resamples randomly from the original distribution of bathymetric data points in the age-defined region. For example, transform fault spacing varies with an average of approximately 50 km between ridge offsets [*Howell et al.*, 2013]. Over a region spanning 8000km ($30°N$ to $-40°S$), a reasonable range of 25-80 km for the offset length scale gives an expected number of independent samples in the range of $N_{bin}=100$ to $N_{bin}=300$ in each bin. This range represents a rough estimate of the minimum number of independent bathymetry measurements necessary to characterize long-wavelength seafloor depth variations in the presence of anomalous short-wavelength topography associated with hot spot swells, transform faulting, and abyssal hills.

To ensure that the results from a single random sample were not anomalous, we performed the K-S test multiple times (1000 runs), with independently bootstrapped data for each run, and averaged the results. By varying the number of samples through a large range of possible independent seafloor bathymetric samples ($N_{KS}$), we find the range of amplitudes of dynamic topography for which the error distributions from regression on the South American flank and prediction on the opposing flanks (Figs. 4 and 5, right columns) produce a statistically-significant P-value ($P < 0.05$, Fig. 6). This range of dynamic topography amplitudes can be considered to produce subsidence patterns on opposite sides of the ridge that are statistically indistinguishable with 95% confidence when observed using the associated number of independent samples (N).  This process

provides a rigorous and repeatable statistical tool to find the amplitudes of dynamic topography that must be removed from maps of residual bathymetry [*Zhong et al.*, 2007], to minimize bathymetric differences across the MOR (Figs. 4 and 5).

We find that runs with fewer samples exhibit systematically higher p-values than runs with more samples (Fig. 6), indicating that the error distributions for the two flanks cannot be distinguished with only sparse sampling, regardless of the amplitude of dynamic topography. This is because the results of the K-S test depend systematically on the number of independent samples. If $N_{bin}$ is small (e.g. 10) the K-S test is less able to distinguish between the two distributions, leading to systematically higher p-values (Fig. 6), as the inherent variance in the bathymetry dominates the K-S test. On the other hand, distributions sampled with a much larger $N_{bin}$ (e.g., 1000) are always distinguishable, and thus produce low p-values (Fig. 6), because any small difference in the distribution becomes statistically meaningful. Therefore, we find that the most useful information from the K-S test is found with $N_{bin}$ between 100 and 300, which concurs with our expectation based on natural length scales.

The results from the K-S tests show that the optimal amount of dynamic topography to minimize ridge asymmetry, as indicated by the range of amplitudes that yield p-values that are highest for a given number of independent samples, are different for the Atlantic and Pacific basins and differ depending on the source of the dynamic topography. The error distributions across the MAR have a broader range of dynamic topography amplitudes for which the two distributions are statistically indistinguishable, compared to the EPR where p-values exhibit a sharper peak (Fig. 6). The total number of samples is greater for the Atlantic, which if the difference in distributions is the same would yield narrower peaks. Thus, the difference is caused by the MAR's more variable bathymetry, which may be due to the greater abundance of small (less than a kilometer in height) seamounts in the Southern Atlantic, as detected by *Kim and Wessel* [2011]. The amount of dynamic

topography required to maximize the p-value, assuming N~300 independent samples, ranges from 100-200 meters sourced from any of the DTBFs in the Pacific basin (Fig. 6, right column), to 400-500 meters for the lower mantle sourced DTBFs in the Atlantic basin (Fig. 6, left column). Moreover, the p-value for the lower mantle DTBFs in both basins can be characterized as non-distinguishable ($p > 0.05$) over a range of dynamic topography amplitudes from 0-600 meters with N in the range of 100 to 300. Taking into account both basins, the maximum of ridge basin symmetry is generated after accounting for 100-500 meters of long-wavelength dynamic topography arising from mantle flow driven by density heterogeneity in the lower mantle (Figs. 4c and 5c).

The upper mantle results differ greatly between the EPR and the MAR, where the Atlantic and Pacific basins constrain the maximum p-value for -400 and +100 meters of dynamic topography, respectively (Fig. 6). The negative dynamic topography constrained in the Atlantic results from the upper mantle DTBFs given by *Conrad and Husson* [2009] (Figs. 3B and 3C), which predict an extension of the downwelling in the Congo basin into the eastern Atlantic basin. This characteristic of the DTBF (Fig. 3C) produces a pattern of dynamic topography opposite to that of the lower mantle (Figs. 3E) and therefore must be applied with opposite sign for dynamic topography to correct the observed bathymetry across the MAR (Fig. 4). Further study is necessary to determine the effect of upper mantle derived dynamic topography, but for the region around the EPR and MAR studied in this paper, shorter wavelength trends are as important. To this point, the effect of UMDN and UMUP offset eachother in the Atlantic basin and almost all observed asymmetry should be derived from lower mantle sourcing. When calculated with the same amount effective R, the total of UMDN and UMUP have a net global amplitude of 600m. This amount of dynamic topography from the upper mantle increases the amplitude necessary from the LMDN source from approximately 400m to 500m, which is within the range given by the K-S test for optimizing symmetry.

**5. Discussion**

In this analysis, we assume that thermal isostatic processes are fully described by seafloor cooling and that any remaining topography is associated with dynamic topography operating across long wavelengths. However, observing the shear wave speed at depths of 36 to 110 km, *Schaeffer and Lebedev* [2013, figure 12] detected a pronounced shear wave slowness of the South American side of the EPR in comparison to the Pacific side. Estimated across the region, shear wave speeds beneath lower lithosphere of the Nazca plate are approximately $120 - 180\ m\ s^{-1}$ slower than they are beneath the Pacific plate [*Ritsema et al.*, 2011; *Schaeffer and Lebedev*, 2013]. This discrepancy suggests that the sub-lithospheric region beneath the Nazca plate is approximately 28°C up to 75°C warmer, assuming *R* in the range 0.15 to 0.4 [*Bull et al.*, 2010]. A lower lithosphere or upper asthenosphere temperature difference of this scale would elevate the South American side of the EPR and potentially mask the dynamic topography signal in the region. Using the relatively simple model of a uniform layer of a given thickness ($H_{layer}$) and of excess temperature ($\Delta T$) under the South American flank of the EPR, we used an isostatic balance,

$$\Delta h = \alpha * H_{layer} * \Delta T * \frac{\rho_{asth}}{(\rho_{asth} - \rho_{water})},$$

to adjust the expected seafloor depth of the South American flank of the EPR, assuming a reasonable thermal expansion coefficient ($\alpha = 3\mathrm{x}10^{-5}\ \mathrm{K}^{-1}$). We considered a range of excess temperature from -30°C to 100°C for a 50 km layer ($H_{layer}$). After applying thermal isostacy, we used the K-S test to find the dynamic topography (model LMDN) that yields the greatest p-value (Fig. 7) for each value of excess temperature.

Our analysis shows that additional dynamic topography is required to ensure symmetry across the EPR, because hotter low-lithosphere temperatures beneath the Nazca lithosphere raises the seafloor and counteracts the vertical deflections from dynamic topography, which tilt the Nazca

seafloor toward South America. For the expected range of excess temperatures, we show that the amplitude of long wavelength dynamic topography necessary to produce EPR asymmetry is about 200-500 m (Fig. 7) for the expected range of possible layer thicknesses (25-100 km) and temperature differences (28°-75°C), consistent with the range we found for the Atlantic Basin. There are several uncertainties in this analysis, including that the thickness of the warm sub-lithospheric layer is uncertain and its temperature anomaly is likely not uniform. However, it is evident that thermal isostatic processes in the asthenosphere can impact our ability to observe dynamic topography on the seafloor [*Molnar et al.*, 2015], even across long-wavelengths.

Our analysis predicts amplitudes of long-wavelength dynamic topography (100-500 m) that are consistent with dynamic topography estimates obtained from gravitational observations [*Molnar et al.*, 2015; *Winterbourne et al.*, 2014], but smaller than those predicted from numerical simulations (~1200 m). This suggests that the seismic conversion factor used by global models such as *Conrad and Husson* [2009] may be too large. As discussed earlier, numerical models of dynamic topography created by *Conrad and Husson* [2009] assume a constant value of the conversion factor between seismic velocity anomaly and density anomaly, $R = 0.21$, for all regions, mineral compositions, and mineral phases in the mantle. Our constraints on the amplitude of dynamic topography suggest that either a smaller value for the conversion factor should be used across the mantle, or that the effective value of $R$ should be reduced in some portions of the mantle, such as the LLSVP regions of the lower mantle.

The ambiguity and apparent longevity of the LLSVPs suggests that using a single value of $R$ for the whole mantle fails to account for the complex behavior of the lower mantle [*Austermann et al.*, 2014; *Deschamps et al.*, 2015]. Indeed, several authors have noted that thermochemical convection and mineral physics associated with the LLSVP regions suggests that a negligible to negative seismic conversion factor, $R <= 0$, applies for low-velocity anomalies in the lower mantle [*Colli et al.*, 2016;

12

*Dannberg and Sobolev*, 2015; *Matas and Bukowinski*, 2007; *McNamara and Zhong*, 2005; *Moulik and Ekström*, 2016] and allows the LLSVPs to be chemically distinct and stable piles [*Wen et al.*, 2001]. Such models of thermochemical convection in the mantle suggest a negligible net contribution to long-wavelength dynamic topography from the LLSVPs, which is consistent with constraints from the geoid that suggest little active upwelling is arising from the lowermost mantle [*Liu and Zhong*, 2016].

Active downwelling and active upwelling driven by density heterogeneity within the lower mantle (LMDN and LMUP), as computed by *Conrad and Husson* [2009], produce similar patterns of dynamic topography (Fig. 3) with similar amplitudes (500 and 530 m, respectively). Our finding that the seafloor is only deflected on long wavelengths at amplitudes of 300-500 meters suggests a contribution from only one of these dynamic topography components. Given that the LLSVP regions may produce little or no active upwelling, we suggest that the observed asymmetry across the mid-ocean ridges is best explained by active downwelling in the lower mantle, with an amplitude similar to those predicted by thermal convection models, but little contribution from active upwelling.

## 6. Conclusions

By comparing subsidence curves on opposing ridge flanks of the MAR and EPR, we show the South American side of both ridges is deeper than the opposing side. This ridge asymmetry can be explained by long-wavelength dynamic topography driven by convection patterns arising from density heterogeneity in the lower mantle. By correcting bathymetry for patterns of dynamic topography predicted using the numerical mantle flow model of *Conrad and Husson* [2009], we found that long-wavelength dynamic topography must have amplitudes of 100-200 meters to explain asymmetry of the EPR and 400-500 meters for the MAR. Such amplitudes are consistent with

amplitudes suggested by the observational studies of *Winterbourne et al.* [2014] and approximately half of the amplitudes suggested by most numerical models of global mantle convection, such as *Conrad and Husson* [2009].

Asymmetry in lower-lithosphere temperature across the EPR, as detected by recent seismic tomography models [e.g., Schaeffer & Lebedev, 2013], may elevate the South American side of the Pacific basin and mask larger-amplitude dynamic topography that would be consistent with our constraints for the Atlantic basin. In this case, asymmetric bathymetry across ridges in the Pacific and Atlantic basins can be explained by long-wavelength dynamic topography with maximum amplitudes of 300-500 meters. Dynamic topography of this amplitude is smaller than that predicted by recent numerical models of purely thermal convection in the mantle, but is consistent with models of thermochemical convection [*Liu and Zhong*, 2016]. In particular, our constraints on dynamic topography suggest that mantle flow is largely driven by active downwelling in the lower mantle, while the LLSVP regions with neutral density anomalies produce little or no active upwelling. Patterns of anomalous long-wavelength bathymetry from across the global seafloor should place important constraints on thermochemical convection models in the future.
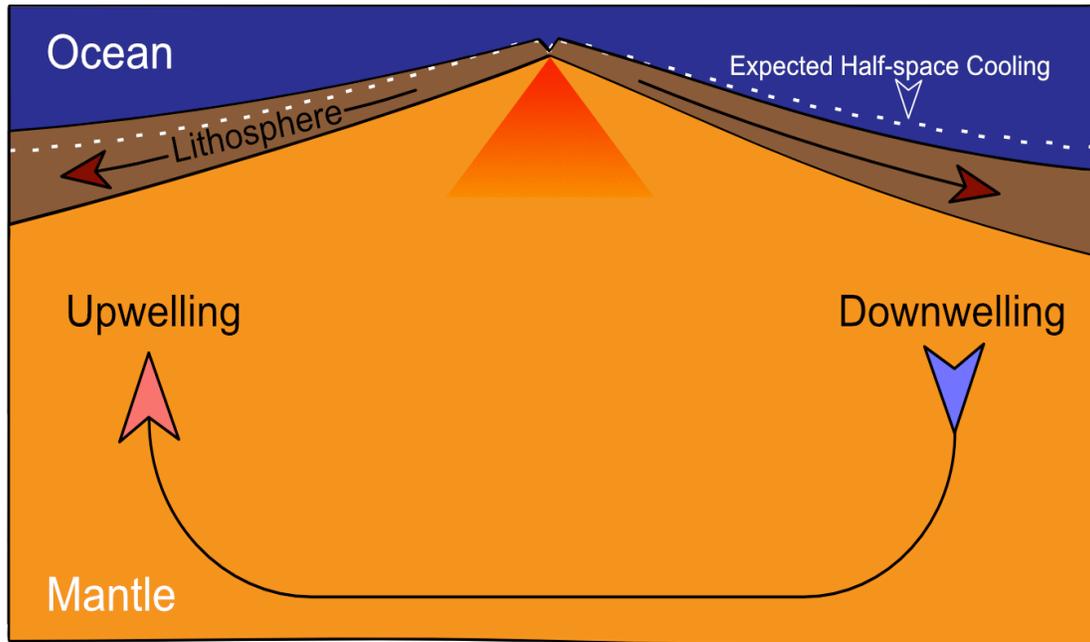
**Figure 1: Cartoon illustrating how stresses from mantle flow** transfer to the Earth's solid surface, creating an apparent asymmetry in half-space cooling across a mid-ocean ridge. The dashed white line represents a symmetric ridge, and the brown ridge shows the seafloor bathymetry after deflection by stresses from mantle flow. In this case, the ridge flank above a downwelling (right) is subsided and the ridge flank above an upwelling (left) is elevated, resulting in a tilted ridge cross section.
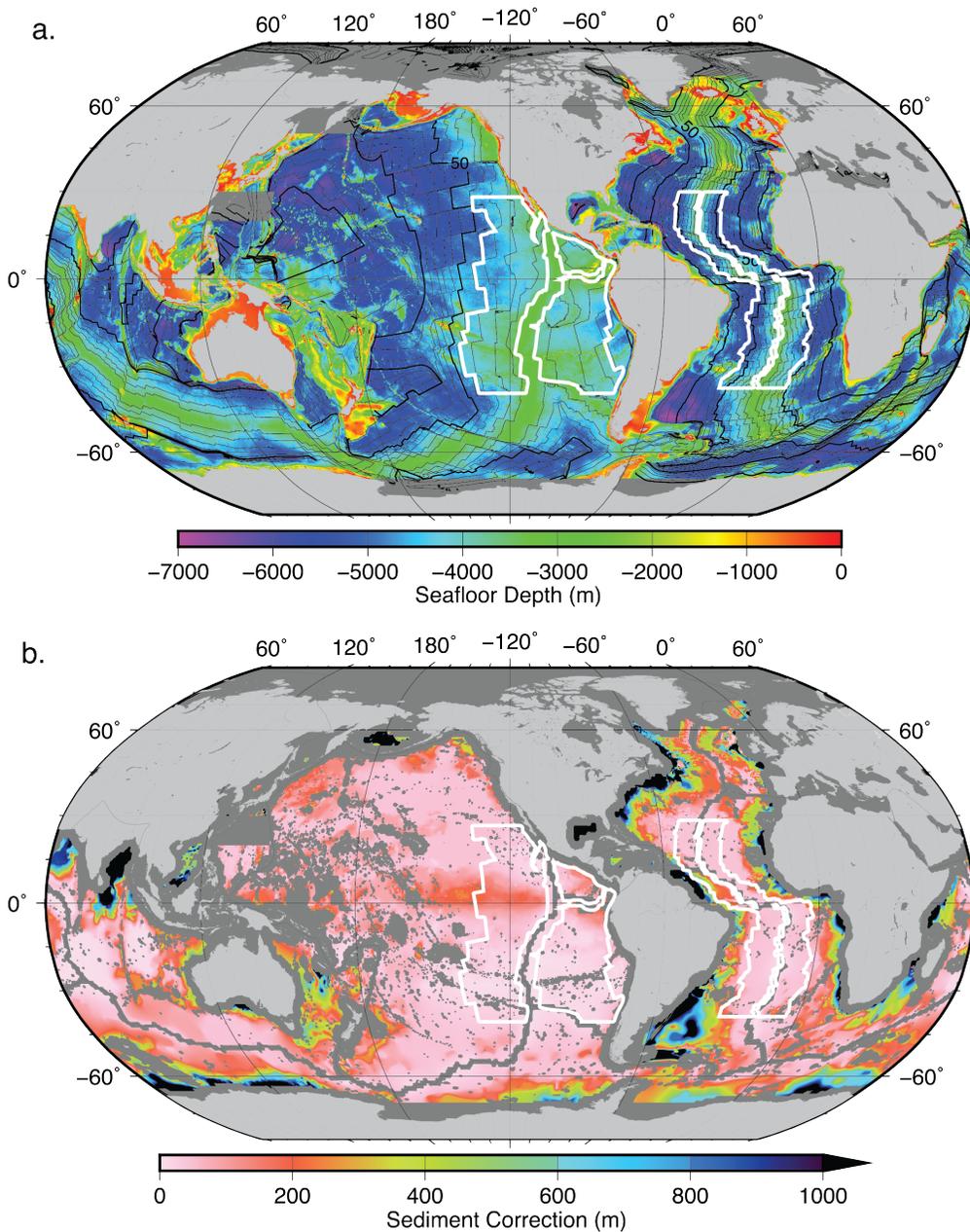
**Figure 2: Maps of seafloor depth, sediment, age, and regions of interest.** (a) Seafloor depth from *Sandwell and Smith* [2009] (shown in colors) and seafloor ages [*Müller et al.*, 2008] (shown by contours with 10 Myr spacing). (b) Sediment depths [*Whittaker et al.*, 2013] are shown in colors, with prescribed regions of hotspots, LIPs, and MORs grayed out. The white outlined areas in both (a) and (b) shows the areas of interest for this study, which straddle the East Pacific Rise (EPR) and Mid-Atlantic Ridge (MAR).

16

# Dynamic Topography Basis Functions

### A) Total Numerical Expecation of Dynamic Topography (m)



### B) Upper–Mantle Upwelling (UMUP, 562m)   C) Upper–Mantle Downwelling (UMDN, 620m)

### D) Lower–Mantle Upwelling (LMUP, 544m)   E) Lower–Mantle Downwelling (LMDN, 530m)

**Normalized Dynamic Topography**
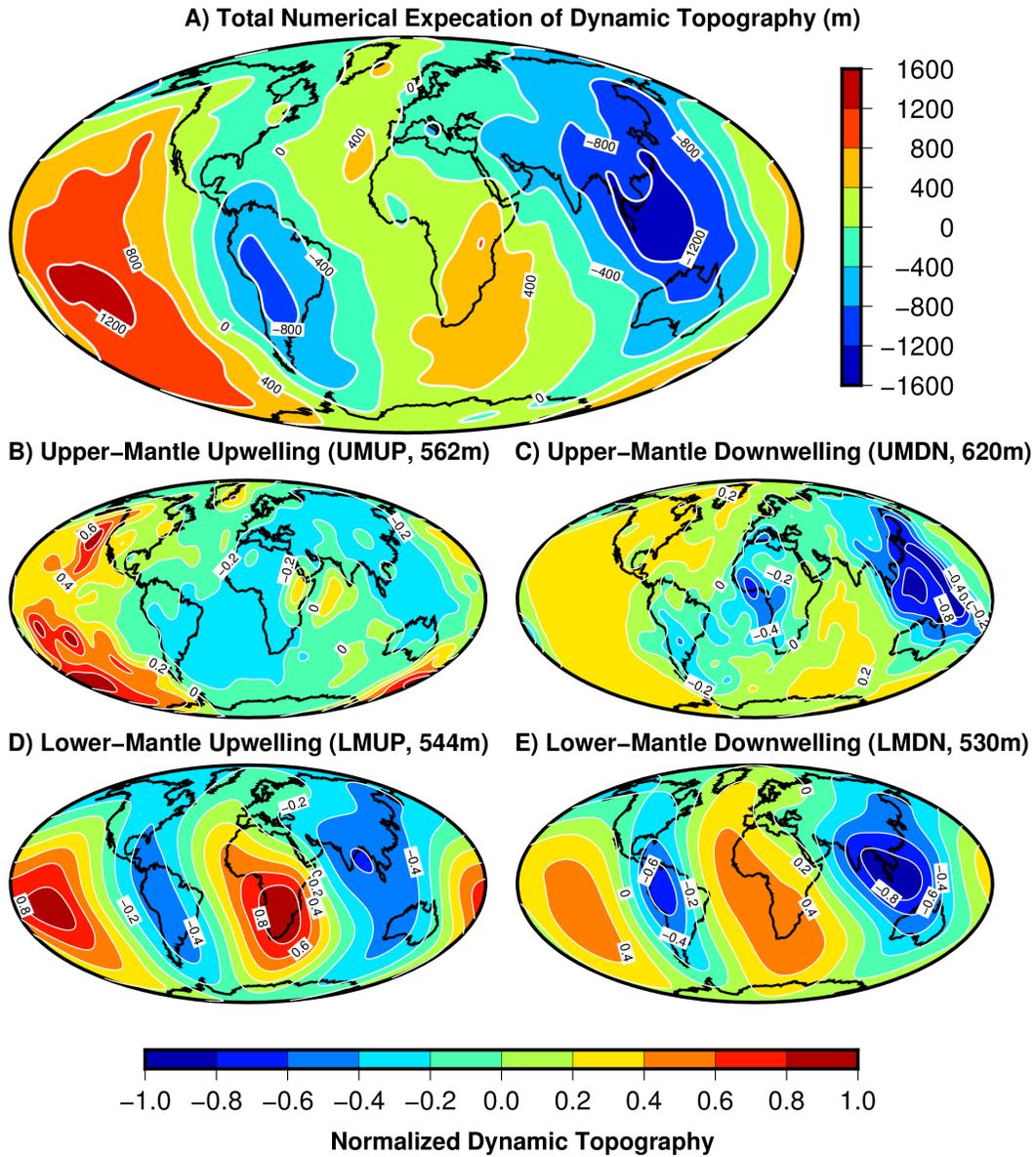
**Figure 3: Dynamic topography predicted by the flow fields from the numerical model** of *Conrad and Husson* [2009], where (A) is the total prediction (whole mantle flow) and (B) through (E) are the dynamic topography basis functions for the components of dynamic topography driven by active upwelling (B and D) or downwelling (C and E) in the upper mantle (B and C) or lower mantle (D and E). These basis functions are normalized by their amplitude such that the maximum absolute value of dynamic topography is unity.
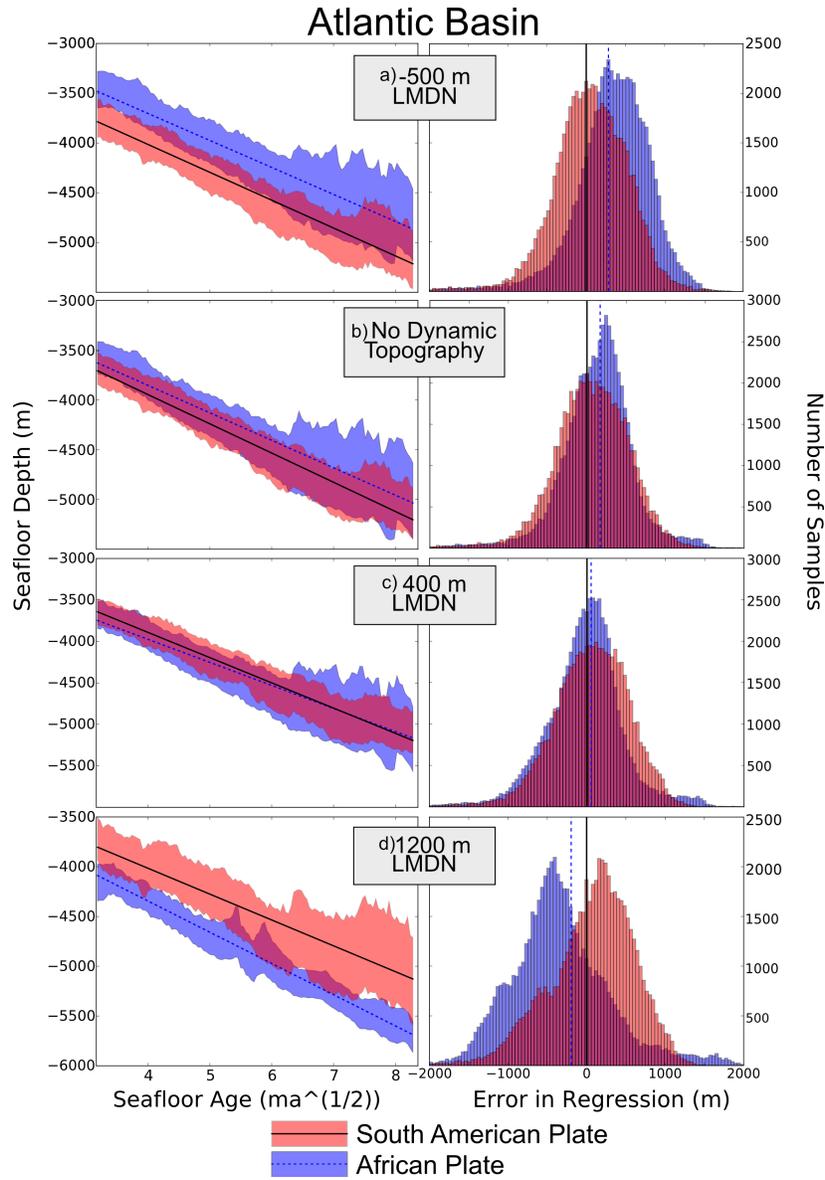
**Figure 4: Comparisons of bathymetric profiles on opposing sides of the Mid-Atlantic Ridge (MAR).** On the left panels, the linear regressions for depth versus square-root of age are the shown by straight lines (black solid for the South American plate and blue dashed for African plate) and the shaded areas representing the standard deviation of data for the bins (light red and blue for the South American and African flanks, respectively). On the right panels, histograms show the bathymetric difference of each point on both sides of the basin relative to the regression developed for the South American flank. In panel-pairs a) through d) we show the effect of first correcting bathymetry for varying amplitudes of dynamic topography produced by active downwelling in the lower mantle (Fig. 3E). We use the distributions represented by these histograms to assess the asymmetry of the ridge basins, using the K-S test (see Fig. 6).
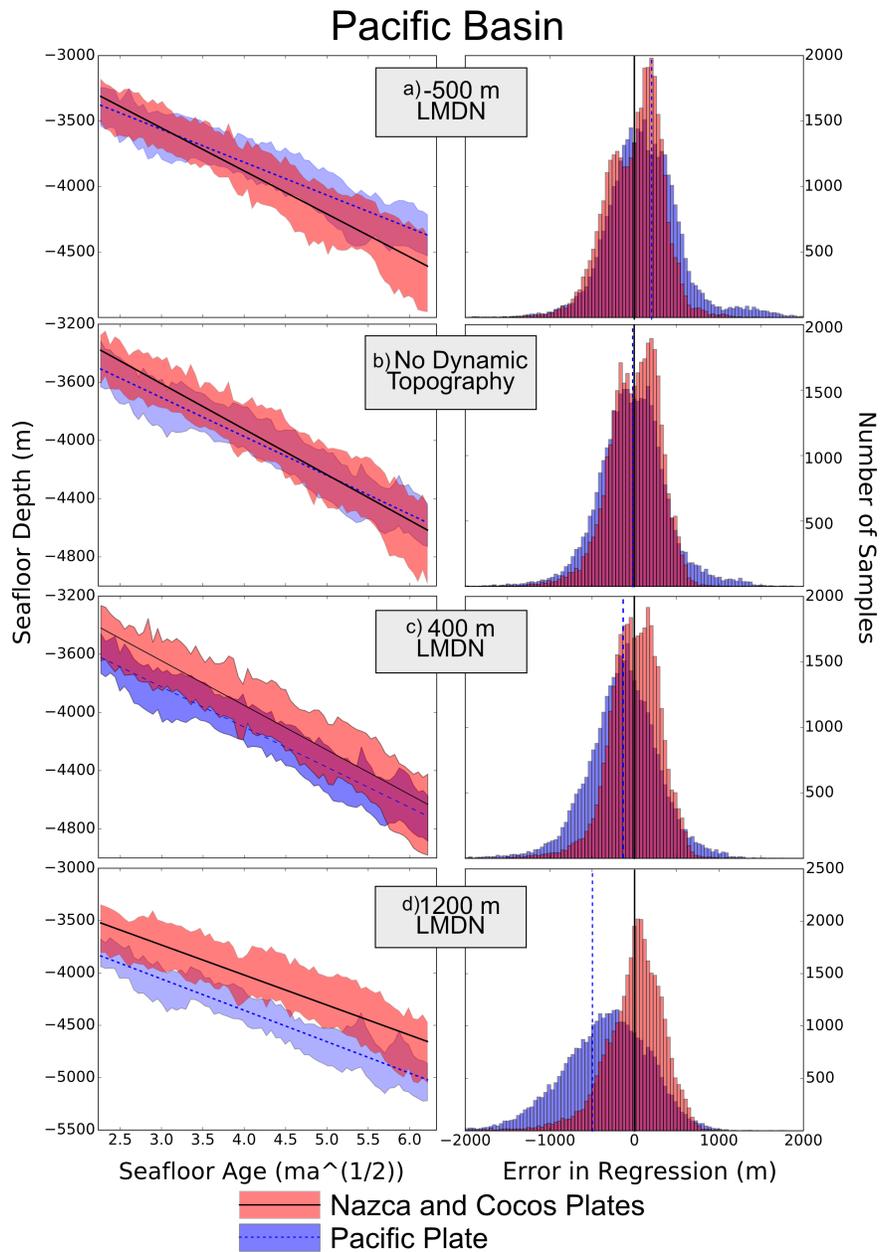
**Figure 5: Comparisons of bathymetric profiles on opposing sides of the East Pacific Rise (EPR).** Similar to Fig. 4, but for the Pacific Basin.
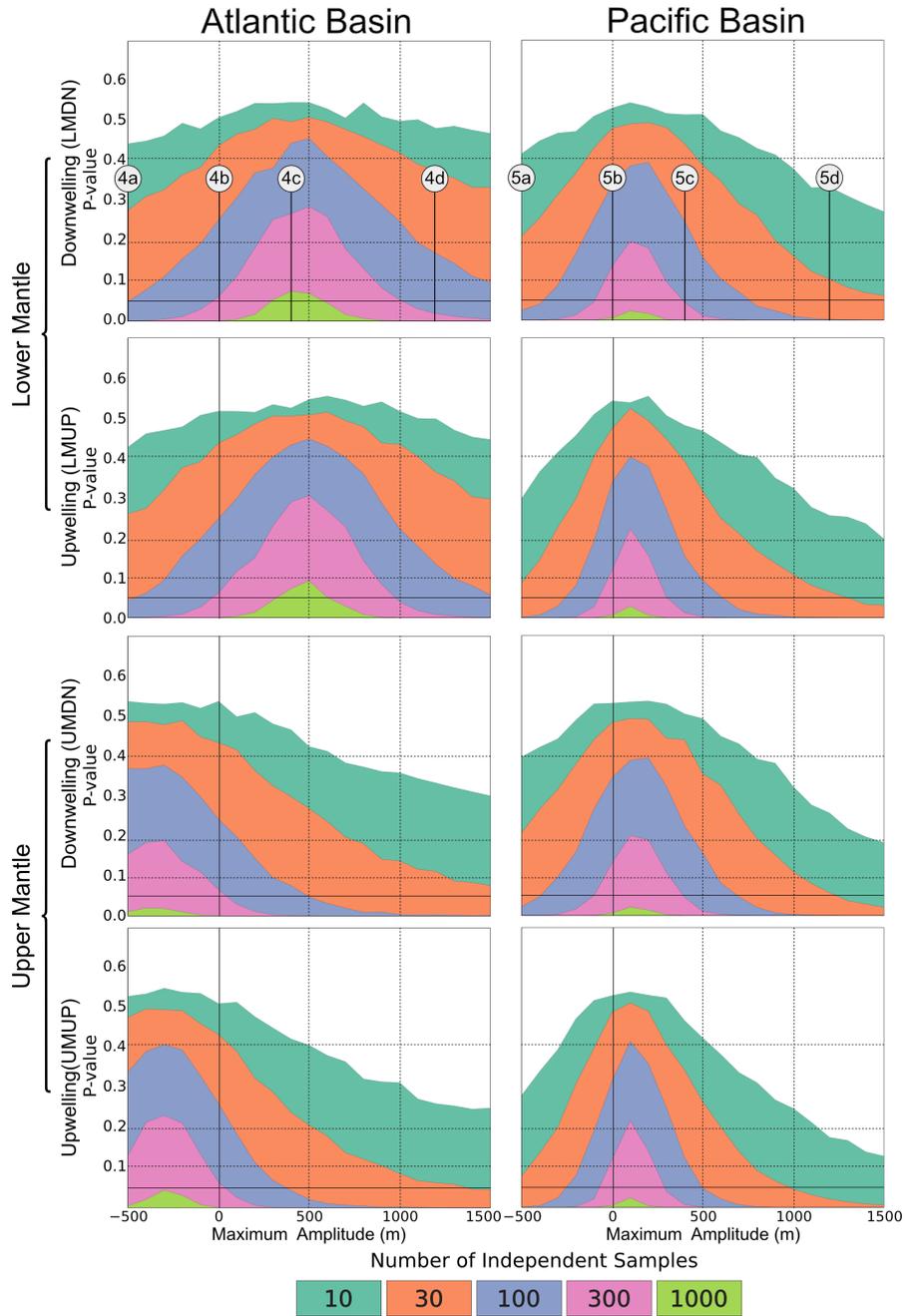
**Figure 6: Application of the two-sample Kolmogorov-Smirnoff (K-S) test** [*Oliphant*, 2007], which we use to quantify the statistical difference between bathymetric distributions of opposing MOR flanks, as a function of the maximum amplitude of dynamic topography removed from the bathymetry (x-axis). We compute the K-S test for the MAR (left column) and the EPR (right column), for each of the four dynamic topography basis functions of Fig. 3 (rows). We compute the p-value of the K-S test for several different values for the number of independent samples ($N_{bin}$ between 10 to 1000 samples per bin) because the appropriate value for $N_{bin}$ is unknown. A larger P-value indicates greater statistical similarity between the distributions. The horizontal black line at P = 0.05 indicates the 95% confidence level; distributions with P-values that fall below this level can be distinguished with 95% confidence.
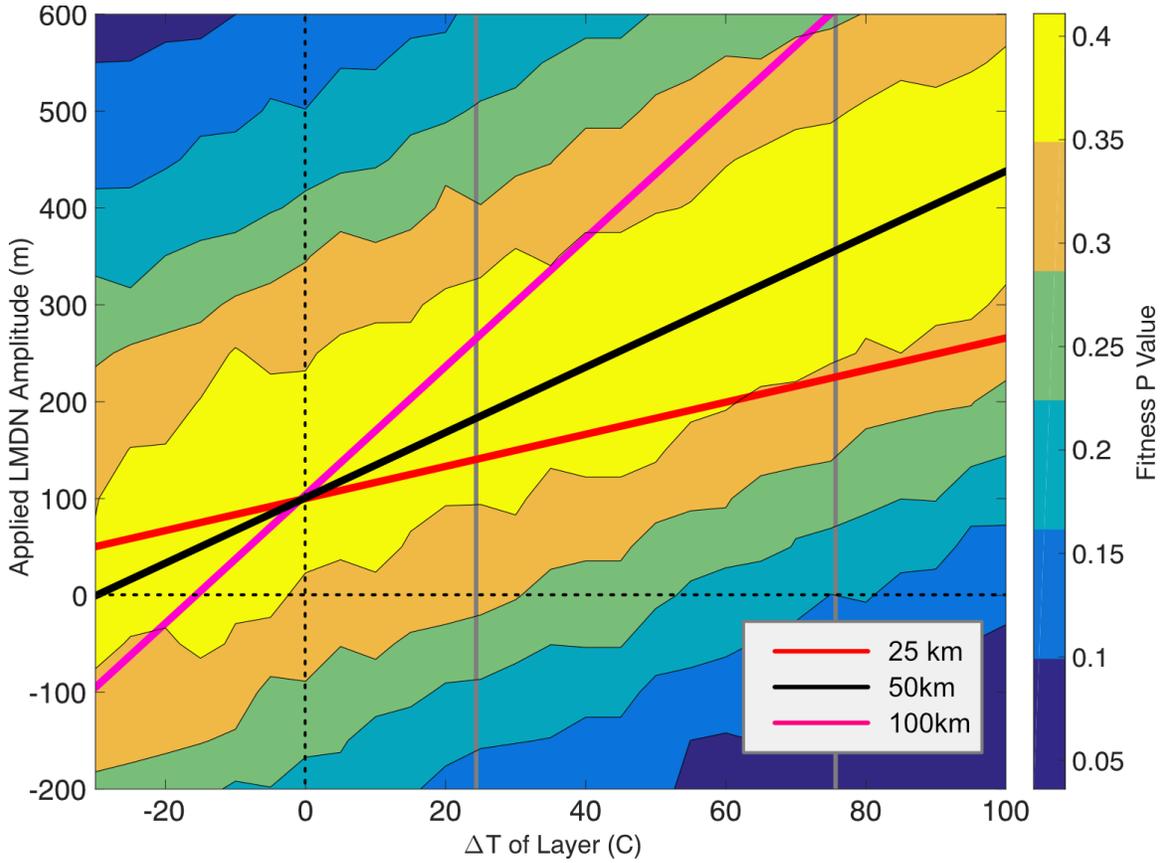
**Figure 7: Maximum p-values (colors) from the K-S test**, computing after correcting EPR bathymetry for LMDN dynamic topography of variable amplitude (y-axis) and isostatic topography arising from a variable sub-lithospheric temperature difference between the two flanks of the ridge (x-axis). Here the background color shows results for a 50 km thick layer, where the maximal p-value is fit by a thick black line. Colored lines show the fit of maximal P-values for separate computations assuming a layer thickness of 25 km (red line) and 100 km (pink line). Grey lines bracket the expected temperature range estimated from the global tomography model of *Schaeffer and Lebedev* [2013].
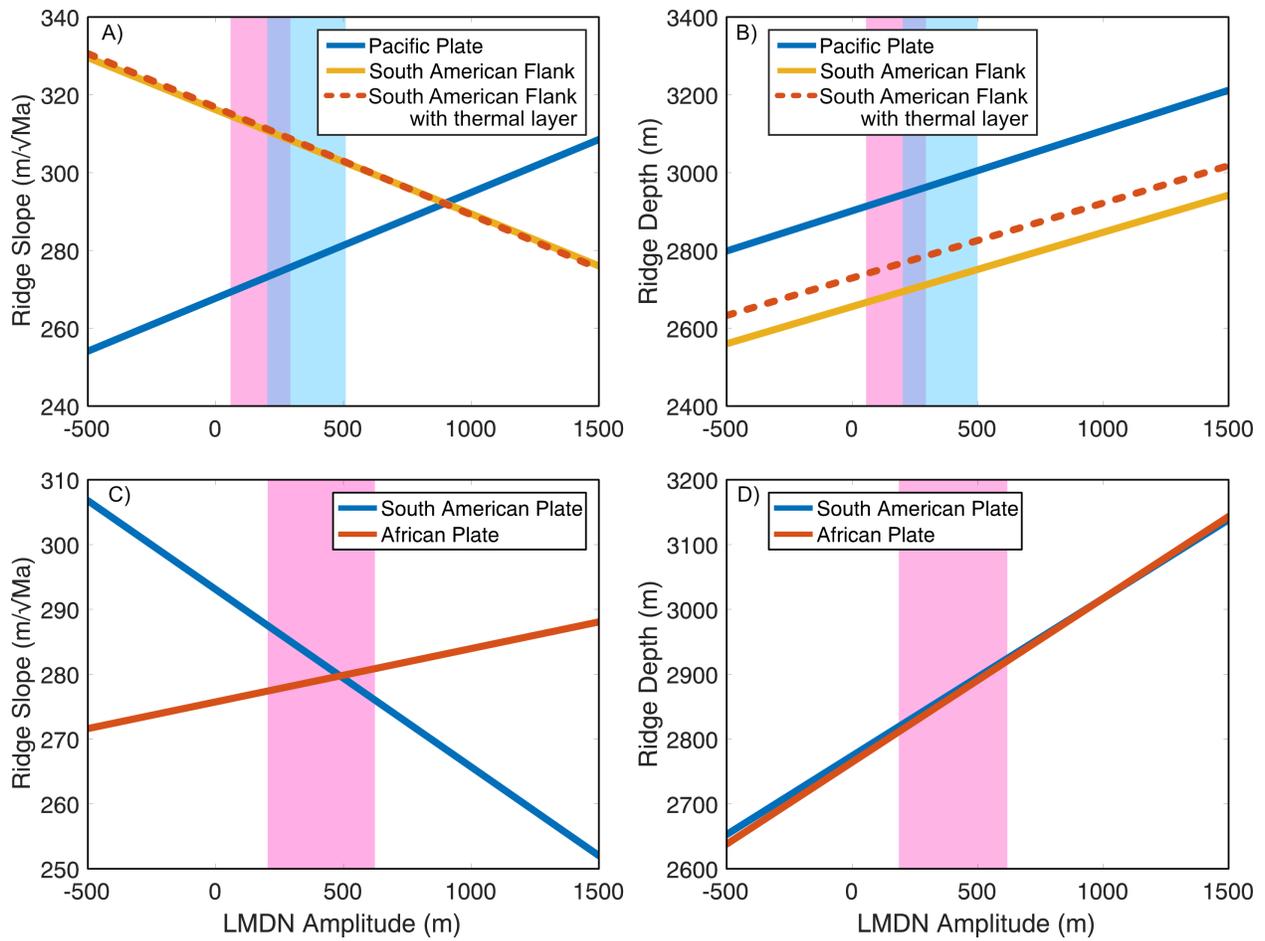
**Figure 8: Ridge subsidence properties after correcting bathymetry for dynamic topography of varying amplitude.** Shown are (A and C) half-space cooling slopes and (B and D) ridge heights for a range of amplitudes of applied dynamic topography from the lower mantle downwelling for the (A and B) Pacific and (C and D) Atlantic basins.

## References

Austermann, J., B. T. Kaye, J. X. Mitrovica, and P. Huybers (2014), A statistical analysis of the correlation between large igneous provinces and lower mantle seismic structure, *Geophysical Journal International*.

Becker, T. W., and R. J. O'Connell (2001), Predicting plate velocities with mantle circulation models, *Geochemistry, Geophysics, Geosystems*, *2*(12), 1060, doi:10.1029/2001GC000171.

Bower, D. J., M. Gurnis, and M. Seton (2013), Lower mantle structure from paleogeographically constrained dynamic Earth models, *Geochemistry, Geophysics, Geosystems*, *14*(1), 44-63, doi:10.1029/2012GC004267.

Bull, A. L., A. K. McNamara, T. W. Becker, and J. Ritsema (2010), Global scale models of the mantle flow field predicted by synthetic tomography models, *Physics of the Earth and Planetary Interiors*, *182*(3–4), 129-138, doi:10.1016/j.pepi.2010.03.004.

Cammarano, F., S. Goes, P. Vacher, and D. Giardini (2003), Inferring upper-mantle temperatures from seismic velocities, *Physics of the Earth and Planetary Interiors*, *138*(3), 197-222.

Coffin, M. F., and O. Eldholm (2005), Large igneous provinces, in *Encyclopedia of Geology*, edited by R. C. Selley, R. Cocks and I. R. Plimer, pp. 315-325, Elsevier, Oxford.

Colli, L., S. Ghelichkhan, and H. P. Bunge (2016), On the ratio of dynamic topography and gravity anomalies in a dynamic Earth, *Geophysical Research Letters*, 2016GL067929, doi:10.1002/2016GL067929.

Conrad, C. P. (2013), The solid Earth's influence on sea level, *Geological Society of America Bulletin*, *125(7-8)*, 1027-1052.

Conrad, C. P., and L. Husson (2009), Influence of dynamic topography on sea level and its rate of change, *Lithosphere*, *1*, 110-120, doi:10.1130/L32.1.

Crosby, A. G. (2007), An assessment of the accuracy of admittance and coherence estimates using synthetic data, *Geophysical Journal International*, *171*(1), 25-54, doi:10.1111/j.1365-246X.2007.03520.x.

Dannberg, J., and S. V. Sobolev (2015), Low-buoyancy thermochemical plumes resolve controversy of classical mantle plume concept, *Nat Commun*, *6*, doi:10.1038/ncomms7960.

Deschamps, F., Y. Li, and P. Tackley (2015), Large-scale thermo-chemical structure of the deep mantle: observations and models, in *The Earth's Heterogeneous Mantle*, edited, pp. 479-515, Springer.

Flament, N., M. Gurnis, and R. D. Mueller (2013), A review of observations and models of dynamic topography, *Lithosphere*(5(2)), 189-210.

Gurnis, M., J. X. Mitrovica, J. Ritsema, and H.-J. van Heijst (2000), Constraining mantle density structure using geological evidence of surface uplift rates: The case of the African Superplume, *Geochemistry, Geophysics, Geosystems*, *1*(7), 1020, doi:10.1029/1999GC000035.

Hager, B. H., R. W. Clayton, M. A. Richards, R. P. Comer, and A. M. Dziewonski (1985), Lower mantle heterogeneity, dynamic topography and the geoid, *Nature*, *313*(6003), 541-545.

Howell, S. M., G. Ito, F. Martinez, M. D. Behn, J. Escartin, and J. L. Olive (2013), Quantifying the variability in tectonic vs. magmatic extension at the Chile Rise, *AGU Fall Meeting Abstracts*, *1*, 03.

Karato, S.-i., and B. B. Karki (2001), Origin of lateral variation of seismic wave velocities and density in the deep mantle, *Journal of Geophysical Research: Solid Earth*, *106*(B10), 21771-21783, doi:10.1029/2001JB000214.

Kim, S.-S., and P. Wessel (2011), New global seamount census from altimetry-derived gravity data, *Geophysical Journal International*, *186*(2), 615-631, doi:10.1111/j.1365-246X.2011.05076.x.

Korenaga, T., and J. Korenaga (2008), Subsidence of normal oceanic lithosphere, apparent thermal expansivity, and seafloor flattening, *Earth and Planetary Science Letters*, *268*(1--2), 41--51.

Lithgow-Bertelloni, C., and P. G. Silver (1998), Dynamic topography, plate driving forces and the African superswell, *Nature*, *395*(6699), 269-272, doi:10.1038/26212.

Liu, and Zhong (2016), Constraining mantle viscosity structure for a thermochemical mantle using the geoid observation, *Geochemistry, Geophysics, Geosystems*, *17*(3), 895-913, doi:10.1002/2015GC006161.

Liu, L. (2015), The ups and downs of North America: Evaluating the role of mantle dynamic topography since the Mesozoic, *Reviews of Geophysics*, *53*(3), 2015RG000489, doi:10.1002/2015RG000489.

Matas, J., and M. S. T. Bukowinski (2007), On the anelastic contribution to the temperature dependence of lower mantle seismic velocities, *Earth and Planetary Science Letters*, *259*(1–2), 51-65, doi:10.1016/j.epsl.2007.04.028.

McNamara, A. K., E. J. Garnero, and S. Rost (2010), Tracking deep mantle reservoirs with ultra-low velocity zones, *Earth and Planetary Science Letters*, *299*(1–2), 1-9, doi:10.1016/j.epsl.2010.07.042.

McNamara, A. K., and S. Zhong (2005), Thermochemical structures beneath Africa and the Pacific Ocean, *Nature*, *437*(7062), 1136-1139.

Molnar, P., P. C. England, and C. H. Jones (2015), Mantle dynamics, isostasy, and the support of high terrain, *Journal of Geophysical Research: Solid Earth*, *120*(3), 2014JB011724.

Moucha, R., A. M. Forte, J. X. Mitrovica, D. B. Rowley, S. Quéré, N. A. Simmons, and S. P. Grand (2008), Dynamic topography and long-term sea-level variations: There is no such thing as a stable continental platform, *Earth and Planetary Science Letters*, *271*(1--4), 101--108.

Moulik, P., and G. Ekström (2016), The relationships between large-scale variations in shear velocity, density, and compressional velocity in the Earth's mantle, *Journal of Geophysical Research: Solid Earth*, *121*(4), 2737-2771, doi:10.1002/2015JB012679.

Müller, R. D., M. Sdrolias, C. Gaina, and W. R. Roest (2008), Age, spreading rates, and spreading asymmetry of the world's ocean crust, *Geochemistry, Geophysics, Geosystems*, *9*(4), 1525-2027, doi:10.1029/2007GC001743.

Oliphant, T. E. (2007), Python for Scientific Computing, *Computing in Science & Engineering*, *9*(3), 10-20, doi:10.1109/MCSE.2007.58.

Olive, J. A., M. D. Behn, G. Ito, W. R. Buck, J. Escartín, and S. Howell (2015), Sensitivity of seafloor bathymetry to climate-driven fluctuations in mid-ocean ridge magma supply, *Science*, *350*(6258), 310-313.

Parsons, B., and J. G. Sclater (1977), An analysis of the variation of ocean floor bathymetry and heat flow with age, *Journal of Geophysical Research*, *82*(5), 803--827.

Revenaugh, J., and B. Parsons (1987), Dynamic topography and gravity anomalies for fluid layers whose viscosity varies exponentially with depth, *Geophysical Journal of the Royal Astronomical Society*, *90*(2), 349-368, doi:10.1111/j.1365-246X.1987.tb00731.x.

Ritsema, A. Deuss, H. J. van Heijst, and J. H. Woodhouse (2011), S40RTS: a degree-40 shear-velocity model for the mantle from new Rayleigh wave dispersion, teleseismic traveltime and normal-mode splitting

function measurements, *Geophysical Journal International*, *184*(3), 1223-1236, doi:10.1111/j.1365-246X.2010.04884.x.

Ritsema, v. Heijst, and Woodhouse (2004), Global transition zone tomography, *Journal of Geophysical Research: Solid Earth*, *109*(B2), n/a-n/a, doi:10.1029/2003JB002610.

Sandwell, D. T., and W. H. F. Smith (2009), Global marine gravity from retracked Geosat and ERS-1 altimetry: Ridge Segmentation versus spreading rate, *J. Geophys. Res*, *114*(B01411,), doi:10.1029/2008JB006008.

Schaeffer, A. J., and S. Lebedev (2013), Global shear speed structure of the upper mantle and transition zone, *Geophysical Journal International*, *194*(1), 417-449.

Shephard, G. E., N. Flament, S. Williams, M. Seton, M. Gurnis, and R. D. Müller (2014), Circum-Arctic mantle structure and long-wavelength topography since the Jurassic, *Journal of Geophysical Research: Solid Earth*, *119*(10), 2014JB011078, doi:10.1002/2014JB011078.

Shephard, G. E., L. Liu, R. D. Müller, and M. Gurnis (2012), Dynamic topography and anomalously negative residual depth of the Argentine Basin, *Gondwana Research*, *22*(2), 658-663, doi:10.1016/j.gr.2011.12.005.

Spasojevic, S., and M. Gurnis (2012), Sea level and vertical motion of continents from dynamic earth models since the Late Cretaceous, *AAPG Bulletin*, *96*(11), 2037-2064, doi:10.1306/03261211121.

Stein, C. A., and S. Stein (1992), A model for the global variation in oceanic depth and heat flow with lithospheric age, *Nature*, *359*(6391), 123--129.

Steinberger, B. (2007), Effects of latent heat release at phase boundaries on flow in the Earth's mantle, phase boundary topography and dynamic topography at the Earth's surface, *Physics of the Earth and Planetary Interiors*, *164*(1–2), 2-20, doi:10.1016/j.pepi.2007.04.021.

Steinberger, B., H. Schmeling, and G. Marquart (2001), Large-scale lithospheric stress field and topography induced by global mantle circulation, *Earth and Planetary Science Letters*, *186*(1), 75-91, doi:10.1016/S0012-821X(01)00229-1.

Sykes, T. J. S. (1996), A correction for sediment load upon the ocean floor: Uniform versus varying sediment density estimations—implications for isostatic correction, *Marine Geology*, *133*(1-2), 35-49, doi:10.1016/0025-3227(96)00016-3.

Tan, E., E. Choi, P. Thoutireddy, M. Gurnis, and M. Aivazis (2006), GeoFramework: Coupling multiple models of mantle convection within a computational framework, *Geochemistry, Geophysics, Geosystems*, *7*(6), n/a-n/a, doi:10.1029/2005GC001155.

van Summeren, J., C. P. Conrad, and C. Lithgow-Bertelloni (2012), The importance of slab pull and a global asthenosphere to plate motions, *Geochemistry, Geophysics, Geosystems*, *13*(2), Q0AK03, doi:10.1029/2011GC003873.

Wen, L., P. Silver, D. James, and R. Kuehnel (2001), Seismic evidence for a thermo-chemical boundary at the base of the Earth's mantle, *Earth and Planetary Science Letters*, *189*(3–4), 141-153, doi:10.1016/S0012-821X(01)00365-X.

Wessel, P., W. H. F. Smith, R. Scharroo, J. Luis, and F. Wobbe (2013), Generic Mapping Tools: Improved Version Released, *Eos, Transactions American Geophysical Union*, *94*(45), 409-410, doi:10.1002/2013EO450001.

Whittaker, J. M., A. Goncharov, S. E. Williams, R. D. Müller, and G. Leitchenkov (2013), Global sediment thickness data set updated for the Australian-Antarctic Southern Ocean, *Geochemistry, Geophysics, Geosystems*, *14*(8), 3297-3305, doi:10.1002/ggge.20181.

Winterbourne, J., N. White, and A. Crosby (2014), Accurate measurements of residual topography from the oceanic realm, *Tectonics*, *33*(6), 982--1015.

Zhong, S., A. McNamara, E. Tan, L. Moresi, and M. Gurnis (2008), A benchmark study on mantle convection in a 3-D spherical shell using CitcomS, *Geochemistry, Geophysics, Geosystems*, *9*(10), n/a-n/a, doi:10.1029/2008GC002048.

Zhong, S., M. Ritzwoller, N. Shapiro, W. Landuyt, J. Huang, and P. Wessel (2007), Bathymetry of the Pacific plate and its implications for thermal evolution of lithosphere and mantle dynamics, *Journal of Geophysical Research: Solid Earth*, *112*(B6), B06412, doi:10.1029/2006JB004628.